PHYSICAL REVIEW B **76**, 064115 (2007)

Indentation of spherical and conical punches into piezoelectric half-space with frictional sliding: Applications to scanning probe microscopy

Arty Makagon* and Mark Kachanov
Department of Mechanical Engineering, Tufts University, Medford, Massachusetts 02155, USA

Sergei V. Kalinin
Materials Sciences and Technology Division, Oak Ridge National Laboratory, Oak Ridge, Tennessee 37831, USA

Edgar Karapetian†
Department of Mathematics & Computer Science, Suffolk University, Boston, Massachusetts, 02114, USA

(Received 26 December 2006; revised manuscript received 20 April 2007; published 21 August 2007)

A proper quantitative interpretation of scanning probe microscopy (SPM) experiments requires solutions for both normal and tangential indentations of punches into a piezoelectric material. Such indentation solutions, their dependence on the indenter shape, and implications for SPM are considered here. More specifically, indentation of the spherical and conically sharp indenters into a piezoelectric half-space accompanied by frictional sliding is addressed. The tangential part of the problem, which involves friction, is solved to complement the solution of the normal indentation problem obtained earlier. Exact stiffness relations between vertical load, tangential displacement, and material properties are obtained. The piezoelectric coupling is found to have a relatively weak effect on lateral contact stiffness. In contrast, the contact area depends noticeably on the tangential effects. The full electroelastic fields are derived in elementary functions and their implications are discussed.

DOI: 10.1103/PhysRevB.76.064115 PACS number(s): 68.35.Gy, 77.84.−s, 77.65.−j, 68.37.Tj

I. INTRODUCTION

The ubiquitous feature of polar inorganic materials having various orientation patterns, as well as phase-separating polymers and biological systems, is the formation of ordered nanoscale regions exhibiting dissimilar electromechanical properties. Examples include ferroelectric and ferroelastic domains in single crystals, grains in piezoelectric and ferroelectric ceramics, phase-separated regions in electroactive polymers, composite structures of connective and calcified tissues, and biopolymers. Understanding and optimization of properties of these materials presents three challenges: (a) real-space imaging of material microstructure and identification of constitutive elements down to the nanometer scale, (b) measurement of local electromechanical properties within a single phase, and (c) understanding the interface properties between the constitutive elements.

Electron microscopy methods, including transmission and scanning electron microscopy, probe local structure based on the differences in local chemical composition and topography. However, they provide no information on the *mechanical* properties. In the last decade, several scanning probe microscopy (SPM) techniques including atomic force acoustic microscopy[1] (AFAM), scanning local acceleration microscopy[2] (SLAM), force modulation microscopy[3] (FMM), hybrid nanoindentation,[4] and ultrasonic force microscopy[5] (UFM) were developed to study the elastic material properties on the nanoscale. Conventional intermittent mode atomic force microscopy provides a wealth of information on the local mechanical properties in the phase image.[6] In parallel, a number of SPM techniques, most notably piezoresponse force microscopy[7] (PFM), were developed to analyze the local electromechanical properties.

PFM has found a broad applicability for the characterization of electromechanically active materials, including imaging domain structures in ferroelectric perovskites, mapping the nanostructure of ferroelectric polymers and biopolymers, and local spectroscopy and polarization switching. In the decade since its invention, PFM has become the primary tool for ferroelectric materials characterization. A recent application of PFM to imaging of biological systems suggests the enormous potential of this technique.[8–10]

These considerations necessitate a fundamental quantitative analysis of contact mechanisms involved in signal generation in PFM, including the effects of lateral tip motion during scanning. This constitutes the primary motivation for the present work. In particular, we address the problem of piezoelectric indentation accompanied by frictional sliding, the motivation being that (i) the sliding motion of the tip on the surface is the inherent feature of contact-mode SPM experiments and (ii) in a number of observations of ferroelectric domains by lateral force microscopy it has been reported that local friction signal provided the contrast that characterizes domain structures. In particular, Eng *et al.*[11] demonstrated that domains in triglycine sulphate (TGS) can be easily visualized in lateral force microscopy (LFM) images, while no contrast is seen in topographic images. Similarly, LFM study of TGS and guanidinium aluminum sulfate hexahydrate (GASH) by Bluhm *et al.*[12] found that friction coefficients were scan-direction and polarization dependent. For the GASH crystal, the LFM contrast was found to be caused by the structural differences between surface domains of different orientations, since the contrast did not invert even if relatively strong bias of 10 V was applied between the sample and the surface. Finally, the disappearance of contrast with temperature across the phase transition was in-

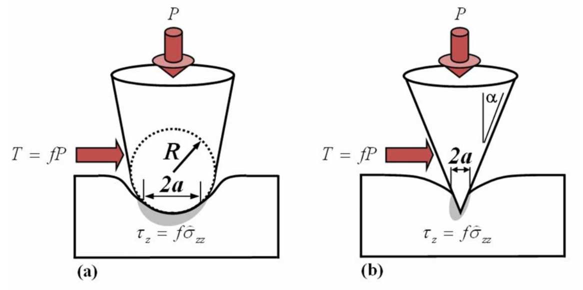

FIG. 1. (Color online) Schematic representation of frictional sliding for (a) spherical and (b) conical indenters.

terpreted by Correia *et al.*[13] as the indicator of its ferroelectric origin.

These studies suggest that the observed contrast is derived from either chemical differences between surfaces of domains with opposite polarity or intrinsic differences in bias-dependent contact mechanics. To resolve this issue, we consider bias effects on the lateral contact mechanics in SPM, and this leads to the problem of indentation of a piezoelectric half-space by a rigid punch accompanied by frictional sliding. Two punch geometries are analyzed: the spherical and the conical ones.

II. FORMULATION OF THE INDENTATION PROBLEM FOR THE PIEZOELECTRIC HALF-SPACE

Problems of piezoelectric indentation present a difficult mathematical challenge. Several solutions for the normal indentation, without friction, have been obtained for the spherical, conical, and flat indenter geometries (Chen[14] and Chen and Ding[15]). In these results, however, the combinations of electroelastic constants in whose terms the fields are expressed are not identified. In works of Giannakopoulos and Suresh[16] and Giannakopoulos,[17] three punch geometries were considered: spherical, conical, and flat circular. In these works, electroelastic fields were given in the closed form on the boundary of the half-space only. Inside the material the fields are given in integral form, which makes it difficult to differentiate between bias and stress effects. Utilizing a recently established correspondence principle (Karapetian *et al.*[18]) between the elastic and piezoelectric problems for transversely isotropic materials, Kalinin *et al.*[19] and Karapetian *et al.*[20] gave the closed-form piezoelectric solution for the spherical, conical, and flat punches.

Here, we consider indentation of the transversely isotropic piezoelectric half-space by the spherical and conical punches where both the normal load P and the shear load in the form of Coulomb's friction, $T=fP$, are applied (see Fig. 1). We use the approximation suggested by Hanson[21,22] in the context of the purely elastic problems, whereby the shear and normal problems are considered to be decoupled. The solution to the purely normal frictionless indentation problems has been given by Karapetian *et al.*[20] The shear problems are solved herein by assuming a shear traction, in the contact region, equal to the normal traction, taken from the normal frictionless indentation problem, multiplied by the friction coefficient f. The full solution is obtained by superimposing the two sets of fields: the purely normal frictionless indentation and the purely lateral frictional sliding. The quality of this approximation is estimated in the text to follow and is found to be good. Moreover, as far as the stiffness relations (punch displacements versus applied forces) are concerned, the obtained solution is exact.

In the present work we follow notations of Karapetian *et al.*[18] The material is transversely isotropic with respect to all three groups of properties (elastic constants, piezoelectric coupling, and dielectric permeabilities), with the z axis being the axis of symmetry. The linear constitutive equations have the form

$$\sigma_{xx} = c_{11}\frac{\partial u_x}{\partial x} + (c_{11} - 2c_{66})\frac{\partial u_y}{\partial y} + c_{13}\frac{\partial u_z}{\partial z} + e_{31}\frac{\partial \phi}{\partial z},$$

$$\sigma_{yy} = (c_{11} - 2c_{66})\frac{\partial u_x}{\partial x} + c_{11}\frac{\partial u_y}{\partial y} + c_{13}\frac{\partial u_z}{\partial z} + e_{31}\frac{\partial \phi}{\partial z},$$

$$\sigma_{zz} = c_{13}\frac{\partial u_x}{\partial x} + c_{13}\frac{\partial u_y}{\partial y} + c_{33}\frac{\partial u_z}{\partial z} + e_{33}\frac{\partial \phi}{\partial z},$$

$$\sigma_{xy} = c_{66}\left(\frac{\partial u_x}{\partial y} + \frac{\partial u_y}{\partial x}\right),$$

$$\sigma_{zx} = c_{44}\left(\frac{\partial u_z}{\partial x} + \frac{\partial u_x}{\partial z}\right) + e_{15}\frac{\partial \phi}{\partial x},$$

$$\sigma_{yz} = c_{44}\left(\frac{\partial u_y}{\partial z} + \frac{\partial u_z}{\partial y}\right) + e_{15}\frac{\partial \phi}{\partial y},$$

$$D_x = e_{15}\left(\frac{\partial u_z}{\partial x} + \frac{\partial u_x}{\partial z}\right) - \varepsilon_{11}\frac{\partial \phi}{\partial x},$$

$$D_y = e_{15}\left(\frac{\partial u_z}{\partial y} + \frac{\partial u_y}{\partial z}\right) - \varepsilon_{11}\frac{\partial \phi}{\partial y},$$

$$D_z = e_{31}\frac{\partial u_x}{\partial x} + e_{31}\frac{\partial u_y}{\partial y} + e_{33}\frac{\partial u_z}{\partial z} - \varepsilon_{33}\frac{\partial \phi}{\partial z}. \qquad (1)$$

For displacements, u_i, stresses, σ_{ij}, electric potential, ψ, and electric displacement components D_i, the following complex notations are introduced:

$$u \equiv u_x + iu_y, \quad u_z, \quad \psi, \quad D \equiv D_x + iD_y, \quad D_z,$$

$$\sigma_1 \equiv \sigma_{xx} + \sigma_{yy}, \quad \sigma_2 \equiv \sigma_{xx} - \sigma_{yy} + 2i\sigma_{xy}, \quad \sigma_{zz},$$
$$\tau_z \equiv \sigma_{zx} + i\sigma_{yz}. \qquad (2)$$

The elastic and piezoelectric constants entering Eq. (1) are as follows: c_{ij} are elastic stiffnesses, e_{ij} are piezoelectric stress constants, ε_{ij} are dielectric permeabilities. Also, the following piezoelectric clusters are widely used: $\alpha_j^* = c_{44}(1+m_j^*) + e_{15}k_j^*$, $\beta_j^* = e_{15}(1+m_j^*) - \varepsilon_{11}k_j^*$ $(j=1,2,3)$, where m_j^*, k_j^* are defined by the following relations:

$$m_j^* = \frac{(c_{11}\gamma_j^{*2} - c_{44})(\varepsilon_{33} - \gamma_j^{*2}\varepsilon_{11}) + \gamma_j^{*2}(e_{15}+e_{31})^2}{(e_{33} - \gamma_j^{*2}e_{15})(e_{15}+e_{31}) + (c_{13}+c_{44})(\varepsilon_{33} - \gamma_j^{*2}\varepsilon_{11})},$$

$$k_j^* = \frac{(c_{11}\gamma_j^{*2} - c_{44})(e_{33} - \gamma_j^{*2}e_{15}) - \gamma_j^{*2}(c_{13}+c_{44})(e_{15}+e_{31})}{(e_{33} - \gamma_j^{*2}e_{15})(e_{15}+e_{31}) + (c_{13}+c_{44})(\varepsilon_{33} - \gamma_j^{*2}\varepsilon_{11})}, \tag{3}$$

where $\gamma_j^{*2} = \lambda_j$ are roots of the cubic equation:

$$A\lambda_j^3 - B\lambda_j^2 + C\lambda_j - D = 0 \tag{4}$$

with coefficients

$$A = c_{11}(c_{44}\varepsilon_{11} + e_{15}^2),$$

$$B = c_{44}[c_{11}\varepsilon_{33} + (e_{15}+e_{31})^2] + \varepsilon_{11}[c_{11}c_{33} + c_{44}^2 - (c_{13}+c_{44})^2] + 2e_{15}[c_{11}e_{33} - (c_{13}+c_{44})(e_{15}+e_{31})] + c_{44}e_{15}^2,$$

$$C = c_{33}[c_{44}\varepsilon_{11} + (e_{15}+e_{31})^2] + \varepsilon_{33}[c_{11}c_{33} + c_{44}^2 - (c_{13}+c_{44})^2] + 2e_{33}[c_{44}e_{15} - (c_{13}+c_{44})(e_{15}+e_{31})] + c_{11}e_{33}^2,$$

$$D = c_{44}(c_{33}\varepsilon_{33} + e_{33}^2). \tag{5}$$

The cubic equation (4) is a consequence of the algebraic equations (Karapetian *et al.*[23])

$$\begin{aligned} \frac{c_{44} + m_j^*(c_{13}+c_{44}) + k_j^*(e_{15}+e_{31})}{c_{11}} &= \frac{m_j^* c_{33} + k_j^* e_{33}}{m_j^* c_{44} + (c_{13}+c_{44}) + k_j^* e_{15}} \\ &= \frac{m_j^* e_{33} - k_j^* \varepsilon_{33}}{m_j^* e_{15} + (e_{15}+e_{31}) - k_j^* \varepsilon_{11}} \\ &= \gamma_j^{*2} \equiv \lambda_j, \quad \gamma_4^* = \sqrt{c_{44}/c_{66}}. \end{aligned} \tag{6}$$

The following clusters of the piezoelectric constants are defined:

$$G_1^* = \beta^* + (e_{15}^2 + c_{44}\varepsilon_{11})\Omega^* H^* = \frac{\gamma_4^*}{2\pi c_{44}} + \frac{\Omega^*}{2\pi \sum_{j=1}^{3} \frac{\alpha_j^* a_j^*}{\gamma_j^{*2}}},$$

$$G_2^* = \beta^* - (e_{15}^2 + c_{44}\varepsilon_{11})\Omega^* H^* = \frac{\gamma_4^*}{2\pi c_{44}} - \frac{\Omega^*}{2\pi \sum_{j=1}^{3} \frac{\alpha_j^* a_j^*}{\gamma_j^{*2}}},$$

$$H^* = \frac{1}{2\pi(e_{15}^2 + c_{44}\varepsilon_{11}) \sum_{j=1}^{3} \frac{\alpha_j^* a_j^*}{\gamma_j^{*2}}},$$

$$\Omega^* = \sum_{j=1}^{3} \frac{a_j^*}{\gamma_j^*} = k_1^*(m_3^* - m_2^*) + k_2^*(m_1^* - m_3^*) + k_3^*(m_2^* - m_1^*),$$

$$a_1^* = \gamma_1^*[(1+m_2^*)k_3^* - (1+m_3^*)k_2^*], \quad 1 \to 2 \to 3 \to 1, \tag{7}$$

and the geometric parameters $(j=1,2,3)$

$$2l_{1j}(z) = \sqrt{(a+\rho)^2 + z_j^2} - \sqrt{(a-\rho)^2 + z_j^2},$$

$$2l_{2j}(z) = \sqrt{(a+\rho)^2 + z_j^2} + \sqrt{(a-\rho)^2 + z_j^2},$$

$$z_j = z/\gamma_j^* \tag{8}$$

are used. Of the clusters (7), the quantity G_1^* plays a particularly important role; as discussed in Sec. VI A, it is the only cluster of piezoelectric constants that enters the stiffness relations. We will also utilize the following relations:

$$\sum_{j=1}^{3} \frac{\alpha_j^* a_j^*}{\gamma_j^*} = \sum_{j=1}^{3} \frac{\beta_j^* a_j^*}{\gamma_j^*} = 0. \tag{9}$$

III. SOLUTION FOR THE SPHERICAL INDENTER

The shear traction in the contact region is taken as a coefficient of friction, $f = f_x + if_y$, multiplied by the normal contact pressure P, so that $T = T_x + T_y = fP$. Thus, the boundary conditions for the shear problem are given as

$$\sigma_{zz} = 0, \quad 0 < \rho < \infty, \quad \tau_z = f\hat{\sigma}_{zz}, \quad \rho \le a,$$

$$\tau_z = 0, \quad \rho > a, \quad D_z = 0, \quad 0 < \rho < \infty, \tag{10}$$

for $0 < \phi < 2\pi$, where $\hat{\sigma}_{zz}$ is taken from the problem of frictionless normal indentation; thus,

$$\tau_z = f\hat{\sigma}_{zz} = \frac{3P(f_x + if_y)}{2\pi a^3}\sqrt{a^2 - \rho^2}. \tag{11}$$

Note that the result used in stating Eq. (11)—the normal traction under the punch for frictionless normal indentation of a piezoelectric half-space—is identical to the corresponding result for the purely elastic isotropic material, earlier obtained by Harding and Sneddon.[24]

A. Full electroelastic fields

The solution is obtained via the correspondence principle that allows constructing the full piezoelectric solution from the purely elastic one. Utilizing the purely elastic solution of Hanson[22] and the correspondence Table 2 of Karapetian *et al.*[18] we obtain coupled electroelastic fields in cylindrical coordinates ρ, ϕ, z as follows:

$$\begin{aligned} u = {} & \frac{3P(G_2^*-G_1^*)}{8a^3\Omega^*}\sum_{j=1}^{3}\frac{a_j^*}{\gamma_j^*}\Biggl\{ f\left[\left(\frac{\rho^2}{2}-a^2-z_j^2\right)\arcsin\left(\frac{l_{1j}}{\rho}\right)+\frac{(2a^2-3l_{1j}^2)(\rho^2-l_{1j}^2)^{1/2}}{2l_{1j}}\right]+\bar{f}e^{2i\phi}\Biggl[-\frac{4a^3z_j}{3\rho^2}+\frac{\rho^2}{4}\arcsin\left(\frac{l_{1j}}{\rho}\right) \\ & +\left[8a^4+a^2\rho^2-l_{1j}^2\left(z_j^2+\frac{5}{2}\rho^2+5a^2\right)\right]\frac{(\rho^2-l_{1j}^2)^{1/2}}{6\rho^2 l_{1j}}\Biggr]\Biggr\} \\ & -\frac{3P(G_2^*+G_1^*)}{8a^3}\Biggl\{ f\left[\left(\frac{\rho^2}{2}-a^2-z_4^2\right)\arcsin\left(\frac{l_{14}}{\rho}\right)+\frac{(2a^2-3l_{14}^2)(\rho^2-l_{14}^2)^{1/2}}{2l_{14}}\right]-\bar{f}e^{2i\phi}\Biggl[-\frac{4a^3z_4}{3\rho^2}+\frac{\rho^2}{4}\arcsin\left(\frac{l_{14}}{\rho}\right) \\ & +\left[8a^4+a^2\rho^2-l_{14}^2\left(z_4^2+\frac{5}{2}\rho^2+5a^2\right)\right]\frac{(\rho^2-l_{14}^2)^{1/2}}{6\rho^2 l_{14}}\Biggr]\Biggr\}, \end{aligned}$$

$$u_z=\frac{3P(G_2^*-G_1^*)}{8a^3\Omega^*}(\bar{f}e^{i\phi}+fe^{-i\phi})\rho\sum_{j=1}^{3}\frac{m_j^*a_j^*}{\gamma_j^{*2}}\left[-z_j\arcsin\left(\frac{l_{1j}}{\rho}\right)+(a^2-l_{1j}^2)^{1/2}\left(1-\frac{l_{1j}^2+2a^2}{3\rho^2}\right)+\frac{2a^3}{3\rho^2}\right],$$

$$\psi=\frac{3P(G_2^*-G_1^*)}{8a^3\Omega^*}(\bar{f}e^{i\phi}+fe^{-i\phi})\rho\sum_{j=1}^{3}\frac{k_j^*a_j^*}{\gamma_j^{*2}}\left[-z_j\arcsin\left(\frac{l_{1j}}{\rho}\right)+(a^2-l_{1j}^2)^{1/2}\left(1-\frac{l_{1j}^2+2a^2}{3\rho^2}\right)+\frac{2a^3}{3\rho^2}\right],$$

$$\sigma_1=\frac{3P(G_2^*-G_1^*)}{4a^3\Omega^*}(\bar{f}e^{i\phi}+fe^{-i\phi})\rho\sum_{j=1}^{3}\left(c_{66}-\frac{\alpha_j^*}{\gamma_j^{*2}}\right)\frac{a_j^*}{\gamma_j^*}\left[-\arcsin\left(\frac{l_{1j}}{\rho}\right)+\frac{l_{1j}(\rho^2-l_{1j}^2)^{1/2}}{\rho^2}\right],$$

$$\begin{aligned} \sigma_2 = {} & \frac{3Pc_{66}(G_2^*-G_1^*)}{2a^3\Omega^*}\sum_{j=1}^{3}\frac{a_j^*}{\gamma_j^*}\Biggl\{ fe^{i\phi}\left[\frac{\rho}{2}\arcsin\left(\frac{l_{1j}}{\rho}\right)-\frac{l_{1j}(\rho^2-l_{1j}^2)^{1/2}}{2\rho}\right]-\bar{f}e^{3i\phi}\left[\frac{4z_j}{3\rho^3}[(l_{1j}^2+2a^2)(a^2-l_{1j}^2)^{1/2}-2a^3]+\frac{l_{1j}^3(\rho^2-l_{1j}^2)^{1/2}}{\rho^3}\right]\Biggr\} \\ & -\frac{3Pc_{66}(G_2^*+G_1^*)}{2a^3}\Biggl\{ fe^{i\phi}\left[\frac{\rho}{2}\arcsin\left(\frac{l_{14}}{\rho}\right)-\frac{l_{14}(\rho^2-l_{14}^2)^{1/2}}{2\rho}\right]+\bar{f}e^{3i\phi}\left[\frac{4z_4}{3\rho^3}[(l_{14}^2+2a^2)(a^2-l_{14}^2)^{1/2}-2a^3]+\frac{l_{14}^3(\rho^2-l_{14}^2)^{1/2}}{\rho^3}\right]\Biggr\}, \end{aligned}$$

$$\sigma_{zz}=\frac{3P(G_2^*-G_1^*)}{8a^3\Omega^*}(\bar{f}e^{i\phi}+fe^{-i\phi})\rho\sum_{j=1}^{3}\frac{\alpha_j^*a_j^*}{\gamma_j^*}\left[-\arcsin\left(\frac{l_{1j}}{\rho}\right)+\frac{l_{1j}(\rho^2-l_{1j}^2)^{1/2}}{\rho^2}\right],$$

$$\begin{aligned} \tau_z = {} & \frac{3P(G_2^*-G_1^*)}{4a^3\Omega^*}\sum_{j=1}^{3}\frac{\alpha_j^*a_j^*}{\gamma_j^{*2}}\left\{ f\left[-z_j\arcsin\left(\frac{l_{1j}}{\rho}\right)+(a^2-l_{1j}^2)^{1/2}\right]-\bar{f}e^{2i\phi}\frac{2a^3-(l_{1j}^2+2a^2)(a^2-l_{1j}^2)^{1/2}}{3\rho^2}\right\} \\ & -\frac{3P}{4\pi a^3}\left\{ f\left[-z_4\arcsin\left(\frac{l_{14}}{\rho}\right)+(a^2-l_{14}^2)^{1/2}\right]+\bar{f}e^{2i\phi}\frac{2a^3-(l_{14}^2+2a^2)(a^2-l_{14}^2)^{1/2}}{3\rho^2}\right\}, \end{aligned}$$

$$D_z=\frac{3P(G_2^*-G_1^*)}{8a^3\Omega^*}(\bar{f}e^{i\phi}+fe^{-i\phi})\rho\sum_{j=1}^{3}\frac{\beta_j^*a_j^*}{\gamma_j^*}\left[-\arcsin\left(\frac{l_{1j}}{\rho}\right)+\frac{l_{1j}(\rho^2-l_{1j}^2)^{1/2}}{\rho^2}\right],$$

$$\begin{aligned} D = {} & \frac{3P(G_2^*-G_1^*)}{4a^3\Omega^*}\sum_{j=1}^{3}\frac{\beta_j^*a_j^*}{\gamma_j^{*2}}\left\{ f\left[-z_j\arcsin\left(\frac{l_{1j}}{\rho}\right)+(a^2-l_{1j}^2)^{1/2}\right]-\bar{f}e^{2i\phi}\frac{2a^3-(l_{1j}^2+2a^2)(a^2-l_{1j}^2)^{1/2}}{3\rho^2}\right\} \\ & -\frac{3P}{4\pi a^3}\frac{e_{15}}{c_{44}}\left\{ f\left[-z_4\arcsin\left(\frac{l_{14}}{\rho}\right)+(a^2-l_{14}^2)^{1/2}\right]+\bar{f}e^{2i\phi}\frac{2a^3-(l_{14}^2+2a^2)(a^2-l_{14}^2)^{1/2}}{3\rho^2}\right\}. \end{aligned} \tag{12}$$

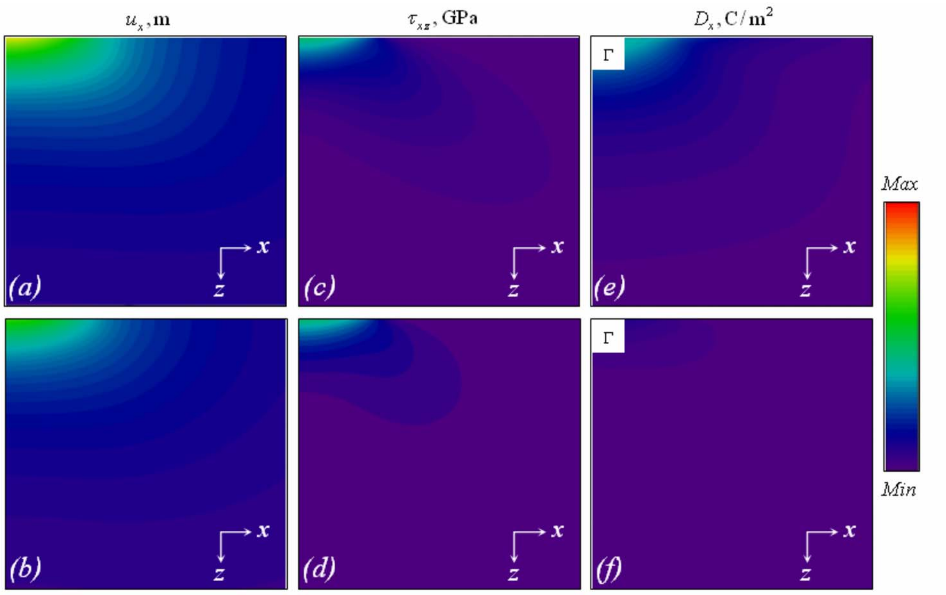

FIG. 2. (Color online) Two-dimensional spatial distribution of the x component of tangential displacement, u_x (a, b), x component of shear stress, τ_{xz} (c), (d), and tangential x component of electric displacement, D_x (e), (f) for spherical indenter geometry for BaTiO$_3$ (a), (c), (e) and LiNbO$_3$ (b), (d), (f). Regions Γ in (c), (f) are scaled up and presented in Fig. 3 below. Indentation parameters are: indentation force $P=1.54$ μN; contact radius $a=3$ nm; coefficient of friction, $f=0.3$; and coordinate $\phi=0$.

The radius a of the contact zone is obtained from the stiffness relation (16) that relates the penetration depth and applied force.

The structure of selected obtained fields is illustrated in Figs. 2 and 3, using material constants for barium titanate (BaTiO$_3$) and lithium niobate (LiNbO$_3$). The relevant clusters of material parameters are given in Table I.

Both the tangential displacement u_x and the shear stress σ_{zx} are maximal directly under the center of the indenter and decrease with increasing x and z. Lines of equal level for u_x attain maximum distance from the origin along the x axis whereas similar lines for σ_{zx} in between the x and z axes. Figure 2 shows that the indenter-induced field of the electric displacement D_x is much weaker for LiNbO$_3$ as compared to BaTiO$_3$, for the reason that the piezoelectric constants e_{ij} are larger for the latter.

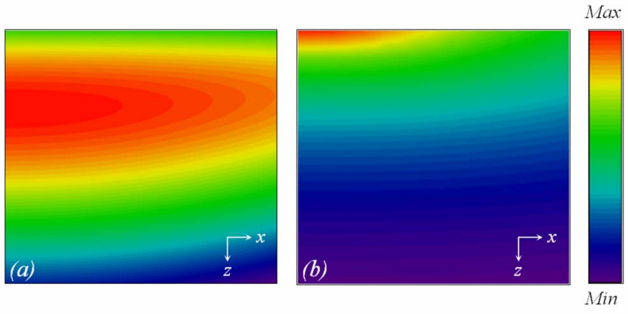

FIG. 3. (Color online) 10× enlargement of region Γ in the spatial distribution of the tangential x component of electric displacement, D_x in Figs. 2(e) and 2(f) for BaTiO$_3$ (a) and LiNbO$_3$ (b). Numerical distribution of the contour plot has been more finely discretized.

As illustrated in Fig. 3(a) (as an enlargement of the zone labeled "Γ" in Fig. 2(e), the maximal value of D_x for BaTiO$_3$ is achieved at certain depth below the surface. This feature is not observed for LiNbO$_3$ [Fig. 3(b), as an enlargement of the zone labeled Γ in Fig. 2(f)]. This difference in behavior of the electric displacement field in the two materials is due to the effect of the cluster of material constants $\frac{c_{44}}{e_{15}}\sum_{j=1}^{3}\frac{\beta_j^* a_j^*}{\gamma_j^{*2}}$ that enters terms A and C in the expression for D_x along the z axis under the center of the indenter ($\rho=0$):

$$D=\frac{-3Pf}{4\pi a^2}\frac{e_{15}}{c_{44}}\left\{\underbrace{\left[\frac{\frac{c_{44}}{e_{15}}\sum_{j=1}^{3}\frac{\beta_j^* a_j^*}{\gamma_j^{*2}}}{\sum_{n=1}^{3}\frac{\alpha_n^* a_n^*}{\gamma_n^{*2}}}+1\right]}_{\boldsymbol{C}}-\left[\underbrace{\frac{\frac{c_{44}}{e_{15}}\sum_{j=1}^{3}\frac{\beta_j^* a_j^*}{\gamma_j^{*2}}\frac{z_j}{a}\sin^{-1}\frac{1}{\sqrt{1+(z_j/a)^2}}}{\sum_{n=1}^{3}\frac{\alpha_n^* a_n^*}{\gamma_n^{*2}}}}_{\boldsymbol{A}}+\underbrace{\frac{z_4}{a}\sin^{-1}\frac{1}{\sqrt{1+(z_4/a)^2}}}_{\boldsymbol{B}}\right]\right\} \qquad (13)$$

This is illustrated by Fig. 4, which shows terms $\boldsymbol{A}$, $\boldsymbol{B}$, and $\boldsymbol{C}$ in Eq. (13) as well as the sum of terms $\boldsymbol{A}$ and $\boldsymbol{B}$ for both materials as a function of material depth. The term $\boldsymbol{C}$ is constant and thus is not a determining factor in the behavior of the electric displacement field.

The difference between the behavior of the two materials is caused by the fact that, for BaTiO$_3$, the ratio (slope of decrease of term $\boldsymbol{A}$)/(slope of increase of term $\boldsymbol{B}$) is larger than 1 near the surface ($z=0$) and decreases to values smaller

TABLE I. Relevant clusters of material constants.

Material	G_1^* (1/GPa)	G_2^* (1/GPa)
BaTiO$_3$	4.913 E-3	1.316 E-3
LiNbO$_3$	4.047 E-3	6.358 E-3

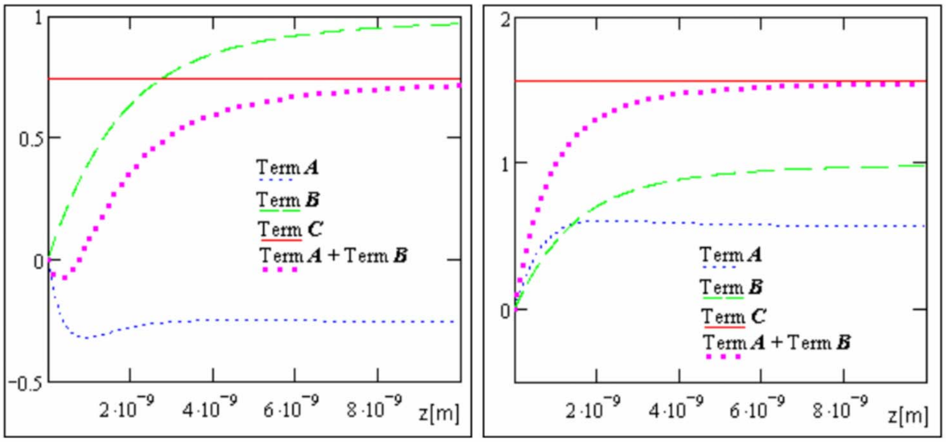

FIG. 4. (Color online) Behavior of terms ***A***, ***B***, and ***C*** entering Eq. (13) and the sum of terms ***A*** and ***B*** for BaTiO$_3$ (a) and LiNbO$_3$ (b).

than 1 with increasing depth. This results in their sum being negative at some depth below the surface and positive at increasing depths asymptotically approaching the value of the term ***C***, such that Eq. (13) goes to zero at infinite depth. Conversely, for LiNbO$_3$, the above-mentioned material property cluster, being opposite in sign to the one for BaTiO$_3$, causes the term ***A*** to increase with depth such that the sum of terms ***A*** and ***B*** is always positive, thereby maximizing Eq. (13) at the surface ($z=0$).

B. Electroelastic fields at the boundary of the half-space

At the boundary of the half-space ($z=0$), the solution obtained above reduces to the following formulas [Eq. (9) is utilized].

(A) At $\rho<a$ ($l_{1j}=\rho$; $l_{2j}=a$),

$$u=\frac{3P\pi}{8a^3}\left[G_1^*f\left(a^2-\frac{\rho^2}{2}\right)+G_2^*\bar{f}e^{2i\phi}\frac{\rho^2}{4}\right],$$

$$u_z=\frac{(G_2^*-G_1^*)P}{4\Omega^*a^3}\left[\frac{a^3-(a^2-\rho^2)^{3/2}}{\rho}\right](\bar{f}e^{i\phi}+fe^{-i\phi})\sum_{j=1}^{3}\frac{m_j^*a_j^*}{\gamma_j^{*2}},$$

$$\psi=\frac{(G_2^*-G_1^*)P}{4\Omega^*a^3}\left[\frac{a^3-(a^2-\rho^2)^{3/2}}{\rho}\right](\bar{f}e^{i\phi}+fe^{-i\phi})\sum_{j=1}^{3}\frac{k_j^*a_j^*}{\gamma_j^{*2}},$$

$$\sigma_1=\frac{3(G_1^*-G_2^*)\pi P}{8\Omega^*a^3}(\bar{f}e^{i\phi}+fe^{-i\phi})\rho\sum_{j=1}^{3}\left(c_{66}-\frac{\alpha_j^*}{\gamma_j^{*2}}\right)\frac{a_j^*}{\gamma_j^*},$$

$$\sigma_2=-\frac{3P\pi G_1^*c_{66}\rho}{4a^3}fe^{i\phi},$$

$$\sigma_{zz}=0,$$

$$\tau_z=-\frac{3P}{2\pi a^3}f(a^2-\rho^2)^{1/2},$$

$$D_z=0,$$

$$D=\frac{3P}{4\pi a^3}\left\{\left[\frac{(G_2^*-G_1^*)\pi}{\Omega^*}\sum_{j=1}^{3}\frac{\beta_j^*a_j^*}{\gamma_j^{*2}}-\frac{e_{15}}{c_{44}}\right]f(a^2-\rho^2)^{1/2}\right.$$
$$+\left[\frac{(G_2^*-G_1^*)\pi}{\Omega^*}\sum_{j=1}^{3}\frac{\beta_j^*a_j^*}{\gamma_j^{*2}}+\frac{e_{15}}{c_{44}}\right]$$
$$\left.\times\bar{f}e^{2i\phi}\frac{(\rho^2+2a^2)(a^2-\rho^2)^{1/2}-2a^3}{3\rho^2}\right\}. \tag{14}$$

(B) At $\rho>a$ ($l_{1j}=a$; $l_{2j}=\rho$),

$$u=\frac{3PG_1^*}{4a^3}\left[f\left(a^2-\frac{\rho^2}{2}\right)\arcsin\left(\frac{a}{\rho}\right)+\frac{a(\rho^2-a^2)^{1/2}}{2}\right]$$
$$+\frac{3PG_2^*}{4a^3}\left[\bar{f}e^{2i\phi}\left(\frac{\rho^2}{4}\right)\arcsin\left(\frac{a}{\rho}\right)\right.$$
$$\left.+a(2a^2-\rho^2)\frac{(\rho^2-a^2)^{1/2}}{4\rho^2}\right],$$

$$u_z=\frac{(G_2^*-G_1^*)P}{4\Omega^*\rho}(\bar{f}e^{i\phi}+fe^{-i\phi})\sum_{j=1}^{3}\frac{m_j^*a_j^*}{\gamma_j^{*2}},$$

$$\psi=\frac{(G_2^*-G_1^*)P}{4\Omega^*\rho}(\bar{f}e^{i\phi}+fe^{-i\phi})\sum_{j=1}^{3}\frac{k_j^*a_j^*}{\gamma_j^{*2}},$$

$$\sigma_1=\frac{3(G_2^*-G_1^*)P}{4\Omega^*a^3}(\bar{f}e^{i\phi}+fe^{-i\phi})\rho\sum_{j=1}^{3}\left(c_{66}-\frac{\alpha_j^*}{\gamma_j^{*2}}\right)$$
$$\times\frac{a_j^*}{\gamma_j^*}\left[\frac{a(\rho^2-a^2)^{1/2}}{\rho^2}-\arcsin\left(\frac{a}{\rho}\right)\right],$$

$$\sigma_2=\frac{3Pc_{66}}{a^3}\left\{G_1^*fe^{i\phi}\left[\frac{a(\rho^2-a^2)^{1/2}}{2\rho}-\frac{\rho}{2}\arcsin\left(\frac{a}{\rho}\right)\right]\right.$$
$$\left.+G_2^*\bar{f}e^{3i\phi}\left[\frac{a^3(a^2-\rho^2)^{1/2}}{\rho^3}\right]\right\},$$

$$\sigma_{zz} = 0,$$

$$\tau_z = 0,$$

$$D_z = 0,$$

$$D = \frac{P\bar{f}e^{2i\phi}}{2\pi\rho^2}\left[\frac{\pi(G_1^* - G_2^*)}{\Omega^*}\sum_{j=1}^{3}\frac{\beta_j^* a_j^*}{\gamma_j^{*2}} - \frac{e_{15}}{c_{44}}\right]. \tag{15}$$

The stiffness relation between the lateral displacement at the punch center u_0 and the tangential force takes the form

$$T = Pf = \frac{8a}{3G_1^*\pi}u_0. \tag{16}$$

This piezoelectric relation is identical to the one for the purely elastic case, provided the cluster G_1^* replaces the combination of elastic constants G_1 (see, for example, Fabrikant[25]).

IV. SOLUTION FOR THE CONICAL INDENTER

Boundary conditions for the spherical indenter apply to the indentation of a cone as well. Based on the solution for the normally loaded conical punch indenting a piezoelectric half-space, the shear traction in the contact zone (related to the normal traction by Coulomb's friction law) is given by

$$\tau_z = f\hat{\sigma}_{zz} = \frac{P(f_x + if_y)}{\pi a^2}\cosh^{-1}\left(\frac{a}{\rho}\right). \tag{17}$$

Importantly, the normal traction distribution in the piezoelectric case, which enters the formula above, is the same as in the purely elastic problem for the isotropic half-space obtained by Sneddon.[26] This fact is discussed in Sec. V of the present work.

A. Full electroelastic fields

Employing the elastic solution of Hanson[21] and utilizing the Correspondence Table 2 of Karapetian *et al.*[18] yields electroelastic fields in cylindrical coordinates ρ, ϕ, z:

$$u = \frac{P(G_2^* - G_1^*)}{2a^2\Omega^*}\sum_{j=1}^{3}\frac{a_j^*}{\gamma_j^*}\left\{f\left[-a\arcsin\left(\frac{l_{1j}}{\rho}\right) - (l_{2j}^2 - a^2)^{1/2} + z_j\ln[l_{2j} + (l_{2j}^2 - \rho^2)^{1/2}]\right.\right.$$
$$\left.\left. + (\rho^2 + z_j^2)^{1/2} - z_j\ln[z_j + (\rho^2 + z_j^2)^{1/2}]\right] + \bar{f}e^{2i\phi}\left[-\frac{a^2 z_j}{\rho^2} + \frac{(\rho^2 + z_j^2)^{3/2} + (4a^2 - 3l_{1j}^2 - l_{2j}^2)(l_{2j}^2 - a^2)^{1/2}}{3\rho^2}\right]\right\}$$

$$- \frac{P(G_2^* + G_1^*)}{2a^2}\left\{f\left[-a\arcsin\left(\frac{l_{14}}{\rho}\right) - (l_{24}^2 - a^2)^{1/2} + z_4\ln[l_{24} + (l_{24}^2 - \rho^2)^{1/2}] + (\rho^2 + z_4^2)^{1/2} - z_4\ln[z_4 + (\rho^2 + z_4^2)^{1/2}]\right]\right.$$
$$\left. - \bar{f}e^{2i\phi}\left[-\frac{a^2 z_4}{\rho^2} + \frac{(\rho^2 + z_4^2)^{3/2} + (4a^2 - 3l_{14}^2 - l_{24}^2)(l_{24}^2 - a^2)^{1/2}}{3\rho^2}\right]\right\},$$

$$u_z = \frac{P(G_2^* - G_1^*)}{2a^2\Omega^*}(\bar{f}e^{i\phi} + fe^{-i\phi})\sum_{j=1}^{3}\frac{m_j^* a_j^*}{\gamma_j^{*2}}\left[\frac{\rho}{2}\ln[l_{2j} + (l_{2j}^2 - \rho^2)^{1/2}] - \frac{\rho}{2}\ln[z_j + (\rho^2 + z_j^2)^{1/2}] + \frac{a^2}{2\rho} - \frac{z_j(\rho^2 + z_j^2)^{1/2}}{2\rho}\right.$$
$$\left. + \frac{(\rho l_{2j} - 2al_{1j})(l_{2j}^2 - \rho^2)^{1/2}}{2\rho^2}\right],$$

$$\psi = \frac{P(G_2^* - G_1^*)}{2a^2\Omega^*}(\bar{f}e^{i\phi} + fe^{-i\phi})\sum_{j=1}^{3}\frac{k_j^* a_j^*}{\gamma_j^{*2}}\left[\frac{\rho}{2}\ln[l_{2j} + (l_{2j}^2 - \rho^2)^{1/2}] - \frac{\rho}{2}\ln[z_j + (\rho^2 + z_j^2)^{1/2}] + \frac{a^2}{2\rho} - \frac{z_j(\rho^2 + z_j^2)^{1/2}}{2\rho}\right.$$
$$\left. + \frac{(\rho l_{2j} - 2al_{1j})(l_{2j}^2 - \rho^2)^{1/2}}{2\rho^2}\right],$$

$$\sigma_1 = \frac{P(G_2^* - G_1^*)}{a^2\Omega^*}(\bar{f}e^{i\phi} + fe^{-i\phi})\sum_{j=1}^{3}\left(c_{66} - \frac{\alpha_j^*}{\gamma_j^{*2}}\right)\frac{a_j^*}{\gamma_j^*}\frac{(l_{2j}^2 - a^2)^{1/2} - (\rho^2 + z_j^2)^{1/2}}{\rho},$$

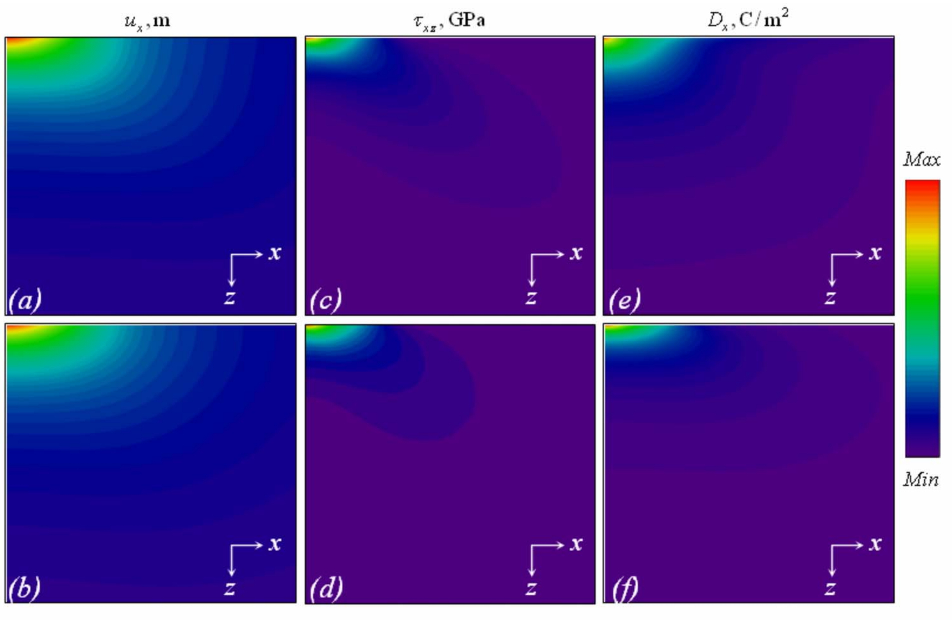

FIG. 5. (Color online) Two-dimensional spatial distribution of the x component of tangential displacement, u_x (a), (b); x component of shear stress, τ_{xz} (c), (d); and tangential x component of electric displacement, D_x (e), (f), for conical indenter geometry for BaTiO$_3$ (a), (c), (e) and LiNbO$_3$ (b), (d), (f). Indentation parameters are indentation force $P=1.54$ μN; contact radius $a=3$ nm; coefficient of friction, $f=0.3$; and coordinate $\phi=0$.

$$\sigma_2 = \frac{Pc_{66}(G_2^* - G_1^*)}{a^2\Omega^*}\sum_{j=1}^{3}\frac{a_j^*}{\gamma_j^*}\left\{fe^{i\phi}\frac{(\rho^2+z_j^2)^{1/2}-(l_{2j}^2-a^2)^{12}}{\rho}+\bar{f}e^{3i\phi}\left[\frac{(12l_{1j}^2+4l_{2j}^2-3\rho^2-16a^2)(l_{2j}^2-a^2)^{1/2}}{3\rho^3}+\frac{4a^2z_j}{\rho^3}\right.\right.$$
$$\left.\left.-\frac{4z_j^2+\rho^4+5z_j^2\rho^2}{3\rho^3(\rho^2+z_j^2)^{1/2}}\right]\right\}-\frac{Pc_{66}(G_2^*+G_1^*)}{a^2}\left\{fe^{i\phi}\frac{(\rho^2+z_4^2)^{1/2}-(l_{24}^2-a^2)^{1/2}}{\rho}-\bar{f}e^{3i\phi}\left[\frac{(12l_{14}^2+4l_{24}^2-3\rho^2-16a^2)(l_{24}^2-a^2)^{1/2}}{3\rho^3}\right.\right.$$
$$\left.\left.+\frac{4a^2z_4}{\rho^3}-\frac{4z_4^2+\rho^4+5z_4^2\rho^2}{3\rho^3(\rho^2+z_4^2)^{1/2}}\right]\right\},$$

$$\sigma_{zz} = \frac{P(G_2^*-G_1^*)}{2a^2\Omega^*}(\bar{f}e^{i\phi}+fe^{-i\phi})\sum_{j=1}^{3}\frac{\alpha_j^*a_j^*}{\gamma_j^*}\frac{(l_{2j}^2-a^2)^{1/2}-(\rho^2+z_j^2)^{12}}{\rho},$$

$$\tau_z = \frac{P(G_2^*-G_1^*)}{2a^2\Omega^*}\sum_{j=1}^{3}\frac{\alpha_j^*a_j^*}{\gamma_j^{*2}}\left\{f\ln\frac{l_{2j}+(l_{2j}^2-\rho^2)^{1/2}}{z_j+(\rho^2+z_j^2)^{12}}+\bar{f}e^{2i\phi}\left[\frac{(2a^2-l_{2j}^2)(a^2-l_{1j}^2)^{1/2}}{a\rho^2}+\frac{z_j(\rho^2+z_j^2)^{1/2}}{\rho^2}-\frac{a^2}{\rho^2}\right]\right\}$$
$$-\frac{P}{2\pi a^2}\left\{f\ln\frac{l_{24}+(l_{24}^2-\rho^2)^{1/2}}{z_4+(\rho^2+z_4^2)^{1/2}}-\bar{f}e^{2i\phi}\left[\frac{(2a^2-l_{24}^2)(a^2-l_{14}^2)^{1/2}}{a\rho^2}+\frac{z_4(\rho^2+z_4^2)^{1/2}}{\rho^2}-\frac{a^2}{\rho^2}\right]\right\},$$

$$D_z = \frac{P(G_2^*-G_1^*)}{2a^2\Omega^*}(\bar{f}e^{i\phi}+fe^{-i\phi})\sum_{j=1}^{3}\frac{\beta_j^*a_j^*}{\gamma_j^*}\frac{(l_{2j}^2-a^2)^{1/2}-(\rho^2+z_j^2)^{1/2}}{\rho},$$

$$D = \frac{P(G_2^*-G_1^*)}{2a^2\Omega^*}\sum_{j=1}^{3}\frac{\beta_j^*a_j^*}{\gamma_j^{*2}}\left\{f\ln\frac{l_{2j}+(l_{2j}^2-\rho^2)^{1/2}}{z_j+(\rho^2+z_j^2)^{1/2}}+\bar{f}e^{2i\phi}\left[\frac{(2a^2-l_{2j}^2)(a^2-l_{1j}^2)^{1/2}}{a\rho^2}+\frac{z_j(\rho^2+z_j^2)^{1/2}}{\rho^2}-\frac{a^2}{\rho^2}\right]\right\}$$
$$-\frac{P}{2\pi a^2}\frac{e_{15}}{c_{44}}\left\{f\ln\frac{l_{24}+(l_{24}^2-\rho^2)^{1/2}}{z_4+(\rho^2+z_4^2)^{1/2}}-\bar{f}e^{2i\phi}\left[\frac{(2a^2-l_{24}^2)(a^2-l_{14}^2)^{1/2}}{a\rho^2}+\frac{z_4(\rho^2+z_4^2)^{1/2}}{\rho^2}-\frac{a^2}{\rho^2}\right]\right\}. \tag{18}$$

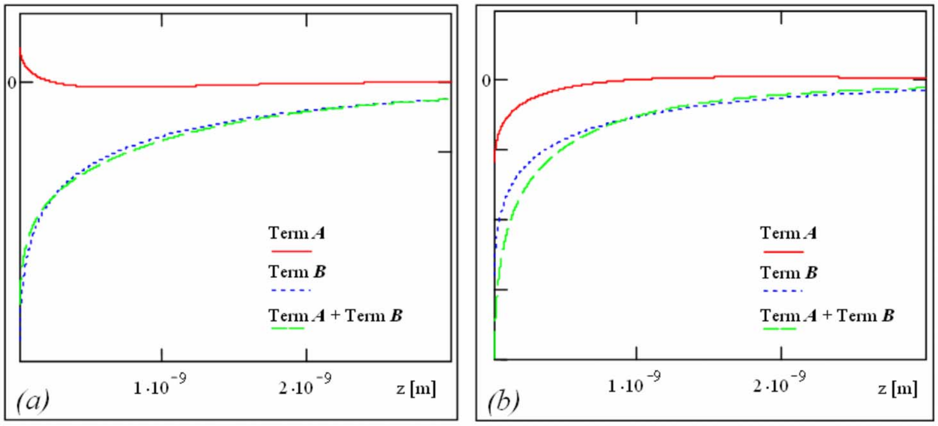

FIG. 6. (Color online) Behavior of terms ***A*** and ***B*** entering Eq. (19) and their sum for $BaTiO_3$ (a) and $LiNbO_3$ (b).

The radius a of the contact zone is obtained from the stiffness relation (22), which relates the penetration depth and applied force.

Selected electroelastic fields for the conical indenter for $BaTiO_3$ and $LiNbO_3$ are shown in Fig. 5. Similar to the case of the spherical indenter, the tangential displacement u_x reaches maximum directly under the center of the indenter and decreases with increasing x and z coordinates. The shear stress σ_{zx} is also maximal on the surface under the center of the indenter and decreases with increasing distance along both axes. In contrast to the displacement field, lines of equal shear stress attain maximum distance from the origin at a point neither on the x nor on the z axes, but rather somewhere in between. The electric displacement field D_x is generally similar to the one for the spherical indenter, with one major difference: *the field reaches a maximum on the surface for both* $BaTiO_3$ *and* $LiNbO_3$ (the maximum electric displacement for $BaTiO_3$ under a spherical indenter is reached at some depth below the material surface).

This is explained by the fact that, close to the center of the punch, for the *conical* indenter, the fields are controlled mostly by the geometric factors (rather than by the material ones), in contrast to the spherical indenter. This produces a singularity at the center of the conical punch. This behavior is depicted in Fig. 5.

These observations are again clarified by the structure of the expression for the electric displacement along the z axis at the center of the indenter ($\rho=0$):

$$D = \frac{-Pf}{2\pi a^2}\frac{e_{15}}{c_{44}}\left\{\underbrace{\left[\sum_{n=1}^{3}\frac{\alpha_n^* a_n^*}{\gamma_n^{*2}}\right]^{-1}\frac{c_{44}}{e_{15}}\sum_{j=1}^{3}\frac{\beta_j^* a_j^*}{\gamma_j^{*2}}\left[\ln\left(\frac{\sqrt{a^2+z_j{}^2}}{z_j}\right)\right]}_{A} + \underbrace{\ln\left(\frac{\sqrt{a^2+z_4{}^2}}{z_4}\right)}_{B}\right\} \tag{19}$$

Figure 6 shows that, for both materials, the term ***B*** is the dominant one, going to negative infinity with decreasing z faster than the ***A*** term goes to positive infinity. Both ***A*** and ***B*** terms contain the logarithmic singularity, but the ***A*** -term has the lessening material property cluster $\frac{c_{44}}{e_{15}}\Sigma_{j=1}^{3}\frac{\beta_j^* a_j^*}{\gamma_j^{*2}}$. Thus, the dominance of the ***B*** term, due to the conical geometry of the punch, requires the maximal value of the sum to be at the surface ($z=0$).

B. Electroelastic fields at the boundary of the half-space

At the boundary of the half-space ($z=0$),the solution takes the following form [Eq. (9) is utilized].

(A) At $\rho < a$ ($l_{1j}=\rho; l_{2j}=a$), we have

$$u = \frac{P}{a^2}\left[G_1^* f\left(\frac{a\pi}{2}-\rho\right) + G_2^* \bar{f} e^{2i\phi}\frac{\rho}{3}\right],$$

$$u_z = \frac{(G_2^* - G_1^*)P}{4\Omega^* a^2}\left[\rho \ln\left(\frac{a-(a^2-\rho^2)^{1/2}}{\rho}\right) + \frac{a^2 - a(a^2-\rho^2)^{1/2}}{\rho}\right] \times (\bar{f}e^{i\phi} + f e^{-i\phi})\sum_{j=1}^{3}\frac{m_j^* a_j^*}{\gamma_j^{*2}},$$

$$\psi = \frac{(G_2^* - G_1^*)P}{4\Omega^* a^2}\left[\rho \ln\left(\frac{a-(a^2-\rho^2)^{1/2}}{\rho}\right) + \frac{a^2 - a(a^2-\rho^2)^{1/2}}{\rho}\right] \times (\bar{f}e^{i\phi} + f e^{-i\phi})\sum_{j=1}^{3}\frac{k_j^* a_j^*}{\gamma_j^{*2}},$$

$$\sigma_1 = \frac{(G_1^* - G_2^*)P}{\Omega^* a^2}(\bar{f}e^{i\phi} + f e^{-i\phi})\sum_{j=1}^{3}\left(c_{66} - \frac{\alpha_j^*}{\gamma_j^{*2}}\right)\frac{a_j^*}{\gamma_j^*},$$

$$\sigma_2 = -\frac{2c_{66}P}{a^2}\left(G_1^* f e^{i\phi} + G_2^* \frac{\bar{f}e^{3i\phi}}{3}\right),$$

$$\sigma_{zz} = 0,$$

$$\tau_z = -\frac{Pf}{\pi a^2}\cosh^{-1}\left(\frac{a}{\rho}\right),$$

$$D_z = 0,$$

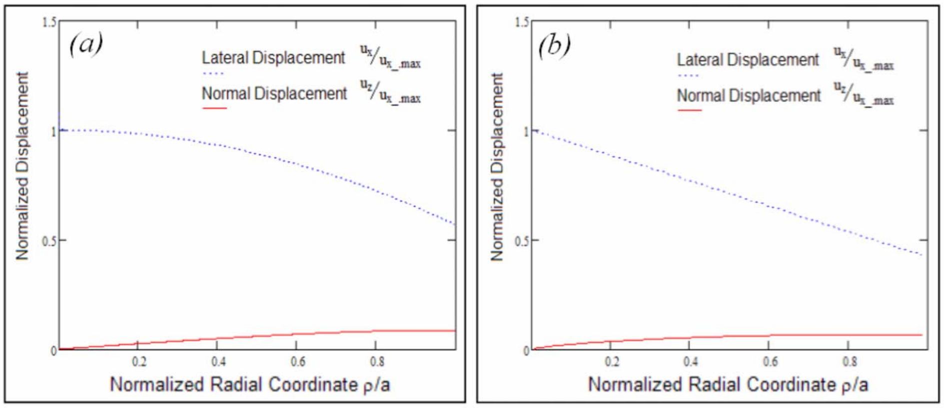

FIG. 7. (Color online) Lateral displacement u_x and normal displacement u_z on the surface ($z=0$) in the contact region for spherical (a) and conical (b) indenters.

$$D = \frac{P}{2\pi a^2}\left\{\left[\frac{(G_2^* - G_1^*)\pi}{\Omega^*}\sum_{j=1}^{3}\frac{\beta_j^* a_j^*}{\gamma_j^{*2}} - \frac{e_{15}}{c_{44}}\right] f \ln \frac{a + (a^2 - \rho^2)^{1/2}}{\rho} + \left[\frac{(G_2^* - G_1^*)\pi}{\Omega^*}\sum_{j=1}^{3}\frac{\beta_j^* a_j^*}{\gamma_j^{*2}} + \frac{e_{15}}{c_{44}}\right]\bar{f} e^{2i\phi}\frac{a(a^2 - \rho^2)^{1/2} - a^2}{\rho^2}\right\}. \tag{20}$$

(B) At $\rho > a$ ($l_{1j}=a; l_{2j}=\rho$), we have

$$u = \frac{P}{a^2}\left\{G_1^* f\left[a \arcsin\left(\frac{a}{\rho}\right) + (\rho^2 - a^2)^{1/2} - \rho\right] + G_2^* \bar{f} e^{2i\phi}\left[\frac{\rho^3 - (\rho^2 - a^2)^{3/2}}{3\rho^2}\right]\right\},$$

$$u_z = \frac{(G_2^* - G_1^*)P}{4\Omega^* \rho}(\bar{f} e^{i\phi} + f e^{-i\phi})\sum_{j=1}^{3}\frac{m_j^* a_j^*}{\gamma_j^{*2}},$$

$$\psi = \frac{(G_2^* - G_1^*)P}{4\Omega^* \rho}(\bar{f} e^{i\phi} + f e^{-i\phi})\sum_{j=1}^{3}\frac{k_j^* a_j^*}{\gamma_j^{*2}},$$

$$\sigma_1 = \frac{(G_2^* - G_1^*)P}{\Omega^* a^2 \rho}[(\rho^2 - a^2)^{1/2} - \rho](\bar{f} e^{i\phi} + f e^{-i\phi}) \times \sum_{j=1}^{3}\left(c_{66} - \frac{\alpha_j^*}{\gamma_j^{*2}}\right)\frac{a_j^*}{\gamma_j^*},$$

$$\sigma_2 = \frac{2c_{66}P}{a^2}\left\{G_1^* f e^{i\phi}\left[\frac{(\rho^2 - a^2)^{1/2} - \rho}{\rho}\right] + G_2^* \frac{\bar{f} e^{3i\phi}}{3}\left[\frac{\rho^3 - (\rho^2 - 4a^2)(\rho^2 - a^2)^{1/2}}{3\rho^3}\right]\right\},$$

$$\sigma_{zz} = 0,$$

$$\tau_z = 0,$$

$$D_z = 0,$$

$$D = \frac{P\bar{f} e^{2i\phi}}{2\pi\rho^2}\left[\frac{\pi(G_1^* - G_2^*)}{\Omega^*}\sum_{j=1}^{3}\frac{\beta_j^* a_j^*}{\gamma_j^{*2}} - \frac{e_{15}}{c_{44}}\right]. \tag{21}$$

The stiffness relation for the conical indenter takes the following form:

$$T = Pf = \frac{2a}{G_1^* \pi} u_0. \tag{22}$$

As in the case of the spherical indenter, the stiffness relation is similar to the one for the purely elastic case, with G_1^* replacing the combination of elastic constants G_1.

V. DISCUSSION OF THE SOLUTIONS

As noted in Sec. II, the piezoelectric fields derived above are approximate for the following reasons.

(i) Stress distributions in the contact zone, for both spherical and conical indenters, are actually different from that for the *normal* frictionless indentation problem alone. Indeed, the normal load required to maintain constant penetration depth during frictional lateral motion is larger than the load required to maintain the same depth in the frictionless normal loading problem.

(ii) The frictional lateral motion actually produces a nonaxisymmetric stress field in the contact zone, while the normal indentation solution observed axial symmetry. The asymmetry is a result of the leading edge of the punch having greater contact area than the trailing edge, to maintain equilibrium.

(iii) The normal displacement on the surface under the punch, u_z, in Eqs. (14) and (20), is nonzero, even though only lateral displacements should be present (as a result of decoupling). The solution becomes exact when the normal displacement on the surface is zero. This occurs when the piezoelectric cluster $\Sigma_{j=1}^{3}\frac{m_j^* a_j^*}{\gamma_j^{*2}}$ entering u_z is zero.

(iv) A zero charge distribution was prescribed in the contact region, but a nonzero electric potential ψ appears in Eqs. (14) and (20). The solution becomes exact when the piezoelectric cluster entering the expression for the electric potential, $\Sigma_{j=1}^{3}\frac{k_j^* a_j^*}{\gamma_j^{*2}}$, is zero.

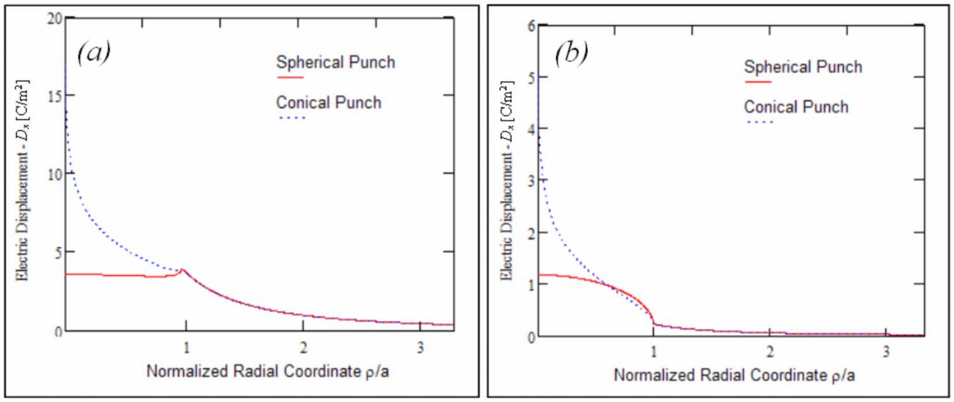

FIG. 8. (Color online) Distribution of the x component of electric displacement, D_x, on the surface ($z=0$) for BaTiO$_3$ (a) and LiNbO$_3$ (b).

To evaluate the quality of the approximations involved in the solution for the lateral problem, we compare the values of the normal and lateral displacements, Fig. 7. It is seen that the normal displacement is an order of magnitude smaller than the lateral one. This indicates that the constructed solution has satisfactory accuracy—on the order of 10%.

An important observation is that the shear traction under the punch on the surface obtained in Secs. III B and IV B is identical to the shear traction for a *purely elastic* isotropic material, as given by Harding and Sneddon[24] and Sneddon[26] and for the transversely isotropic material as well (Green and Zerna[27]). Therefore, as far as the contact problems discussed here are concerned, the difference between the purely elastic and the piezoelectric materials is observed only at nonzero depth, provided that the punch is electrically grounded (electrical boundary conditions are set to null).

Another observation is that for a punch subjected to a given load, the radius of the contact a is a function of the radius of curvature, R, for a spherical punch or the semiangle α of the cone for the conical punch (Fig. 1). Larger R and α would result in a larger radius of contact and smaller lateral displacement. Note, also, that electric displacements on the surface outside of the contact zone are independent of the punch geometry, Fig. 8.

Note that the stiffness relations for both spherical and conical geometries, as given by Eqs. (16) and (22), appear to be independent of charge. This is a consequence of the fact that zero charge was specified as a boundary condition. However, the charge is actually delegated to the normal frictionless problem and enters the full solution via superposition of the two problems assumed in the present work. Here, we superimpose the stiffness relations obtained above with the ones from the previously solved normal frictionless indentation problem to obtain the full stiffness relations for the spherical,

$$P = \frac{8a}{3G_1^* \pi f} u_0 + \frac{4aC_1^*}{3\pi} w_0 + \frac{2aC_3^*}{\pi} \psi_0,$$

$$Q = -\frac{4aC_3^*}{3\pi} w_0 + \frac{2aC_4^*}{\pi} \psi_0, \tag{23}$$

and conical indenters,

$$P = \frac{2a}{G_1^* \pi f} u_0 + \frac{2C_1^* \tan \alpha}{\pi^2} (w_0 + \varepsilon)^2 + \frac{2aC_3^*}{\pi} \psi_0,$$

$$Q = -\frac{2C_3^* \tan \alpha}{\pi^2} (w_0 + \varepsilon)^2 + \frac{2aC_4^*}{\pi} \psi_0, \tag{24}$$

under normal and lateral load with tip bias, given in Eqs. (23) and (24), respectively.

Equations (23) and (24) illustrate that, due to the manner in which the problem was decoupled, the mechanical load P is a function of the friction coefficient f, while the electric charge is independent of friction. Note that the limiting case of the purely elastic problems (considered by Hanson[21,22]) is recovered from our results by setting the piezoelectric coupling constants $e_{ij}=0$, with the following replacement of the constants:

$$m_3^*, k_1^*, k_2^* \to 0, \quad \gamma_3^* \to \sqrt{\varepsilon_{33}/\varepsilon_{11}}, \quad \gamma_4^* \to \gamma_3 = \sqrt{c_{44}/c_{66}}.$$

Remark. In the literature, the lateral stiffness relation has not always been used correctly. For example, Cain *et al.*,[28] Carpick *et al.*,[29] and Lantz *et al.*[30] took the lateral stiffness relation from the decoupled solution of Johnson.[31] This solution, suggested in the absence of exact results, is based on the assumptions that it is valid to decouple the normal and shear modes and that the shear traction distribution under the *bonded* punch coincides with the normal traction distribution under the *frictionless* ("smooth") punch. An exact coupled solution became available later[25] and showed that Johnson's assumptions led to substantial error. However, these considerations do not necessarily invalidate the experimental studies. Indeed, in the studies of Cain *et al.*,[28] Carpick *et al.*,[29] and Lantz *et al.*,[30] which were focused on friction force microscopy (FFM) calibration, the potential numerical error in the contact stiffness equation may be offset by the "effective" contact area of the probe as defined during calibration.

VI. STRUCTURE OF STIFFNESS RELATIONS AND EFFECT OF MATERIALS PROPERTIES

In this section, we analyze stiffness relations for the spherical and conical indenters and the relation to the PFM contact mechanics and imaging mechanism.

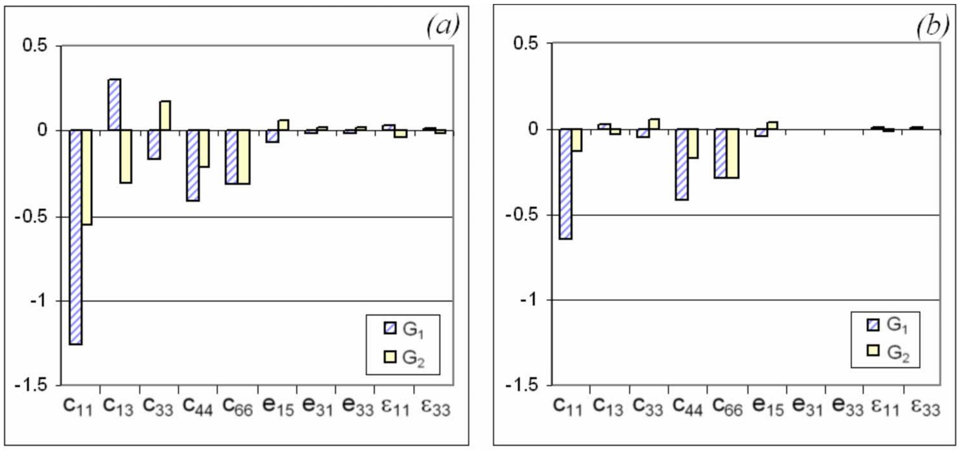

FIG. 9. (Color online) Sensitivity function of the piezoelectric clusters G_1^*, G_2^* to the elastic stiffnesses, electroelastic coupling constants, and dielectric permiabilities of which they are comprised for $BaTiO_3$ (a) and $LiNbO_3$ (b).

A. Discussion of the stiffness relations

We now analyze the stiffness relations that relate the applied lateral force T and the lateral displacement at the punch center u_0 (as derived in Secs. III and IV) and have the form, for the spherical and the conical indenters,

$$T = \frac{8a}{3G_1^* \pi} u_0 \quad \text{(spherical)},$$

$$T = \frac{2a}{G_1^* \pi} u_0 \quad \text{(conical)}. \tag{25}$$

We consider the dependence of the piezoelectric constant cluster G_1^* entering these relations, as well as the associated cluster G_2^*, given by Eq. (7), on their ten constituent independent piezoelectric constants: five elastic stiffnesses c_{ij}, three electroelastic coupling constants e_{ij}, and two dielectric permeabilities ε_{ij}. In order to identify the relative contribution of each piezoelectric constant to a cluster G_k^*, a sensitivity function of that cluster is defined as the logarithmic derivative of G_k^* with respect to a selected piezoelectric constant f_{ij} as follows: $S_k(f_{ij}) = \delta[\ln(G_k^*)]/\delta[\ln(f_{ij})]$. Numerically, the sensitivity function is calculated as

$$S_k(f_{ij}) = \frac{G_k^*|_{f_{ij}=1.01 f_{ij}^0} - G_k^*|_{f_{ij}=0.99 f_{ij}^0}}{0.02\ G_k^*|_{f_{ij}=f_{ij}^0}}, \tag{26}$$

where f_{ij} is a selected piezoelectric constant and f_{ij}^0 is a reference value for that constant. A positive value of $S_k(f_{ij})$ implies that a higher constant value favors a cluster increase, while for negative values of $S_k(f_{ij})$ the cluster decreases with the constant. $S_k(f_{ij}) \approx 0$ indicates that the cluster is independent of that property. The sensitivity of clusters G_k^* for $BaTiO_3$ and $LiNbO_3$ to the ten independent material constants is shown in Figs. 9(a) and 9(b), respectively.

The sensitivity analysis indicates that material property clusters G_1^*, G_2^* are primarily determined by the elastic stiffness coefficients and are only weakly dependent on the piezoelectric constants and dielectric permeabilities.

B. Nanoelectromechanics of lateral SPM

In PFM the measured quantity—the piezoresponse amplitude—is the voltage derivative of the tip-surface displacement, $PR = (\partial w_0 / \partial \psi_0)_{P=const.}$. From the stiffness relations, Eqs. (23) and (24), the PFM signal in the presence of the lateral displacement u_0 and the piezoresponse amplitude acquire the form

$$PR = \frac{2 w_0 C_3^*}{2 w_0 C_1^* + C_3^* \psi_0}[1 - K],$$

$$K = \left[1 + \frac{3 G_1^* f}{4 u_0}(2 w_0 C_1^* + C_3^* \psi_0)\right]^{-1}, \tag{27a}$$

$$PR = \frac{2 a^2 C_3^*}{2 a^2 C_1^* + C_3^* \psi_0 R}[1 - K],$$

$$K = \left[1 + \frac{2 a f}{R T \pi}(2 a^2 C_1^* + C_3^* \psi_0 R)\right]^{-1}, \tag{27b}$$

for the spherical indenter, and

$$PR = \frac{(w_0 + \varepsilon) C_3^*}{C_1^* (w_0 + \varepsilon) + C_3^* \psi_0}[1 - K],$$

$$K = \left[1 + \frac{G_1^* f}{u_0}[C_1^* (w_0 + \varepsilon) + C_3^* \psi_0]\right]^{-1}, \tag{28a}$$

$$PR = \frac{a \cot(\alpha) \pi C_3^*}{C_1^* a \cot(\alpha) \pi + 2 C_3^* \psi_0}[1 - K],$$

$$K = \left[1 + \frac{a f}{T \pi}[C_1^* a \cot(\alpha) \pi + 2 C_3^* \psi_0]\right]^{-1}, \tag{28b}$$

for the conical indenter. The coefficient in Eqs. (27) and (28) corresponds to the piezoresponse signal in the absence of lateral force. Lateral force acting on a tip during the scanning will result in decrease of the measured electromechanical response. For typical parameters in a PFM experiment using BTO $(a = 3\ \text{nm}, R = 50\ \text{nm}, \psi_0 = 1\ \text{V}, T = 30\ \text{nN}, f = 0.3)$ the magnitude of K for a spherical indenter is 0.18. This indicates the relative importance of the lateral displacement contribution to the piezorespose amplitude.

A similar analysis for the quantity measured in atomic force acoustic microscopy, $k_1=(\partial w_0/\partial P)_{\psi_0=const}$—the inverse vertical spring constant of the tip-surface junction—yields

$$k_1 = \frac{\pi\sqrt{w_0}}{\sqrt{R}(2w_0C_1^* + C_3^*\psi_0)}[1-K],$$
$$K = \left[1 + \frac{3G_1^* f}{4u_0}(2w_0C_1^* + C_3^*\psi_0)\right]^{-1}, \qquad (29a)$$

$$k_1 = \frac{\pi a}{2a^2C_1^* + RC_3^*\psi_0}[1-K],$$
$$K = \left[1 + \frac{2af}{RT\pi}(2a^2C_1^* + C_3^*\psi_0 R)\right]^{-1}, \qquad (29b)$$

for the spherical indenter, and

$$k_1 = \frac{(w_0+\varepsilon)\pi}{2aC_1^*(w_0+\varepsilon) + 2aC_3^*\psi_0}[1-K],$$
$$K = \left[1 + \frac{G_1^* f}{u_0}[C_1^*(w_0+\varepsilon) + C_3^*\psi_0]\right]^{-1}, \qquad (30a)$$

$$k_1 = \frac{\cot(\alpha)\pi^2}{2C_1^* a\cot(\alpha)\pi + 4C_3^*\psi_0}[1-K],$$
$$K = \left[1 + \frac{af}{T\pi}[C_1^* a\cot(\alpha)\pi + 2C_3^*\psi_0]\right]^{-1}, \qquad (30b)$$

for the conical indenter.

Finally, to complement PFM, AFAM can be used to measure the voltage-dependent lateral contact stiffness of tip surface junction. From Eq. (25), the lateral contact stiffness depends only on the effective contact area and does not explicitly depend on tip bias. However, the contact area is bias dependent from Eq. (23) and (24), as analyzed in detail in Kalinin *et al.*[19] Hence, the lateral contact stiffness can be used as a measure of bias-dependent contact area in PFM, suggesting a route for independent measurement of the latter.

VII. CONCLUSIONS

The piezoelectric indentation of punches of spherical and conical shapes into a piezoelectric half-space accompanied by frictional sliding is analyzed. The obtained solutions, derived in elementary functions, give the full electroelastic fields in explicit form, as well as exact stiffness relations. These results form the basis for quantification of SPM techniques for ferroelectric and piezoelectric materials. The problem is solved under the approximation whereby the normal and the tangential parts of the problem are decoupled. Estimates show that this assumption is satisfactory, with errors on the order of 10%. The present work focuses on the tangential part of the problem; the normal one has been solved previously.

The main results relevant for SPM applications are as follows.

(i) The lateral contact stiffness does not explicitly depend on indenter bias and is determined only by the radius of contact.

(ii) The effective piezoelectric shear modulus is primarily determined by the elastic material constants, while piezoelectric and dielectric constants provide only minor contributions.

(iii) The presence of lateral displacement results in a decrease of indentation depth, thus reducing piezoresponse at a given indentation force.

The present work suggests important applications for interpretation of various scanning probe microscopy techniques of ferroelectric surfaces. First, measurements of the lateral contact stiffness using lateral AFAM or FFM can provide an independent method to establish the voltage-dependent contact area for subsequent use in PFM (i.e., to calibrate the contact area between the probe and the surface). Second, the friction force is expected to be only weakly dependent on piezoelectric and dielectric material properties at zero tip bias. Hence, the observed friction contrast on ferroelectric domains is likely attributed to variations in polarization-dependent chemical properties, rather than intrinsic polarization response. At the same time, application of finite voltage bias will result in strong changes in effective contact area, and hence the friction force will be domain polarity dependent. For positive domains, the contact area decreases for positive tip biases, with associated decrease of friction force, and increases for negative bias. The situation is reversed for negative domains. Hence, friction force measurements under dc tip bias can provide direct imaging of domain polarity. Finally, we mention that the solution presented here assumes that during experimentation the indenter tip velocities are constant or exhibit relatively low acceleration.

ACKNOWLEDGMENT

This research has been supported by the National Science Foundation through a grant to Tufts University (No. CMS-0509936).

---

*Corresponding author. arty.makagon@tufts.edu

†Corresponding author. edgark@mcs.suffolk.edu

[1] U. Rabe, V. Sherer, S. Hirsekorn, and W. Arnold, J. Vac. Sci. Technol. B **15**, 1506 (1997).

[2] N. A. Burnham, A. J. Kulik, G. Gremaud, P.-J. Gallo, and F. Oulevey, J. Vac. Sci. Technol. B **14**, 794 (1996).

[3] P. Maivald, H. J. Butt, S. A. C. Gould, C. B. Prater, B. Drake, J. A. Gurley, V. B. Elings, and P. K. Hansma, Nanotechnology **2**,

103 (1991).

[4] S. A. Syed Asif, K. J. Wahl, R. J. Colton, and O. L. Warren, J. Appl. Phys. **90**, 1192 (2001).

[5] K. Yamanaka, H. Ogiso, and O. Kolosov, Appl. Phys. Lett. **64**, 178 (1994).

[6] *Applied Scanning Probe Methods*, edited by B. Bhushan, H. Fuchs, and S. Hosaka (Springer-Verlag, Berlin, 2004).

[7] *Nanoscale Characterization of Ferroelectric Materials*, edited by M. Alexe, and A. Gruverman (Springer-Verlag, Berlin, 2004).

[8] C. Halperin, S. Mutchnik, A. Agronin, M. Molotskii, P. Urenski, M. Salai, and G. Rosenman, Nano Lett. **4**, 1253 (2004).

[9] J. Shin, B. J. Rodriguez, A. P. Baddorf, T. Thundat, E. Karapetian, M. Kachanov, A. Gruverman, and S. V. Kalinin, J. Vac. Sci. Technol. B **23**, 2102 (2005).

[10] S. V. Kalinin, B. J. Rodriguez, S. Jesse, T. Thundat, and A. Gruverman, Appl. Phys. Lett. **87**, 053901 (2005).

[11] L. M. Eng, M. Friedrich, J. Fousek, and P. Gunter, J. Vac. Sci. Technol. B **14**, 1191 (1996).

[12] H. Bluhm, U. D. Schwarz, and R. Wiesendanger, Phys. Rev. B **57**, 161 (1998).

[13] A. Correia, J. Massanell, N. Garcia, A. P. Levanyuk, A. Zlatkin, and J. Przeslawski, Appl. Phys. Lett. **68**, 2796 (1996).

[14] W. Q. Chen, Arch. Appl. Mech. **69**, 455 (1999).

[15] W. Q. Chen and H. Ding, Acta Mech. Sol. Sin. **12**, 114 (1999).

[16] A. E. Giannakopoulos and S. Suresh, Adv. Mater. (Weinheim, Ger.) **47**, 2153 (1999).

[17] A. E. Giannakopoulos, J. Appl. Mech. **67**, 409 (2000).

[18] E. Karapetian, M. Kachanov, and I. Sevostianov, Arch. Appl. Mech. **72**, 564 (2002).

[19] S. V. Kalinin, E. Karapetian, and M. Kachanov, Phys. Rev. B **70**, 184101 (2004).

[20] E. Karapetian, M. Kachanov, and S. V. Kalinin, Philos. Mag. B **85**, 1017 (2005).

[21] M. Hanson, J. Appl. Mech. **59**, S123 (1992).

[22] M. Hanson, ASME J. Tribol. **114**, 606 (1992).

[23] E. Karapetian, I. Sevostianov, and M. Kachanov, Philos. Mag. B **80**, 331 (2000).

[24] W. Harding and I. N. Sneddon, Proc. Cambridge Philos. Soc. **41**, 16 (1945).

[25] V. I. Fabrikant, *Applications of Potential Theory in Mechanics* (Kluwer, Dordrecht, 1989).

[26] I. N. Sneddon, Proc. Cambridge Philos. Soc. **44**, 492 (1948).

[27] A. E. Green and W. Zerna, *Theoretical Elasticity* (Oxford University Press, London, 1968).

[28] R. G. Cain, S. Briggs, and N. W. Page, J. Colloid Interface Sci. **227**, 55 (2000).

[29] R. W. Carpick, D. F. Ogletree, and M. Salmeron, Appl. Phys. Lett. **70**, 1548 (1997).

[30] M. A. Lantz, A. J. O'shea, A. C. F. Hoole, and M. E. Welland, Appl. Phys. Lett. **70**, 970 (1997).

[31] K. L. Johnson, *Contact Mechanics* (Cambridge University Press, Cambridge, England, 1969).